Seismic imaging of complex geometry: forward modeling of sandstone intrusions

Antonio Grippa [a,*], Andrew Hurst [a], Giuseppe Palladino [a], David Iacopini [a], Isabelle Lecomte [b], Mads Huuse [c]

[a] Department of Geology and Petroleum Geology, University of Aberdeen, Aberdeen, UK

[b] Department of Earth Science, University of Bergen, Bergen, Norway

[c] School of Earth and Environmental Sciences, University of Manchester, Manchester, UK

* Corresponding author. E-mail address: antonio.grippa@abdn.ac.uk (A. Grippa)

Keywords: seismic forward modeling; sandstone intrusion; tuning wedge; discordant contacts; waste sequestration; vertical transmissivity

Abstract

Sandstone intrusions form large bedding-discordant sandstones that intruded into finer grained, less permeable host strata. They form naturally sand-propped hydraulic fractures that constitute a connected network of permeable conduits through which fluids escape to the Earth's surface. Saucer-shaped sandstone intrusions are among the largest volume intrusions and are commonly resolved on seismic data. Outcrop analogues of seismically-resolved saucers-shaped intrusions reveal that many attendant intrusions, in particular dikes, are undetected in seismic data. Seismic forward modeling of a detailed outcrop description of a saucer-shaped intrusion demonstrates that intrusions steeper than 45º are undetected and that up to 40% of the entire volume of sandstone intrusions is not seismically imaged. Wedge geometry associated with discordant contacts between different lithologies causes constructive and destructive amplitude interference, creating imaging artefacts of sandstone thickness and geometry. Comparison of the outcrop seismic models with 3D seismic data from Volund oilfield demonstrate both the similarity of the saucer-shaped intrusions and the

distribution and quantity of dikes that may be undetected (ca. 78%) using subsurface data. Lack of detection of dikes has direct implications on the valuation of upward migration of fluids and an overestimation of seal capacity. This therefore has major implications when using seismic data to evaluate waste sequestration or to execute hydrocarbon or groundwater exploration and production.

1. Introduction

Interpretation of seismic images is integral to the evaluation of the significance of shallow crustal fluid-migration systems in fine-grained strata (Hurst et al., 2003; Huuse et al., 2010; Blackford et al., 2014; Karstens and Berndt, 2015; Cevatoglu et al., 2016). Identification of complex geological features is however compromised by the limits of resolution (Moser and Howard, 2008) and bedding-discordant features, (*e. g.* sandstone dikes) which are notoriously difficult to image. Consequently, when using seismic images to evaluate the transmissivity of fine-grained strata - seals in petroleum systems (Cartwright et al., 2007) - important permeable conduits may be undetected and the seal capacity overestimated. Extensional fractures and faults periodically or permanently enhance fluid transmissivity through intrinsically low-permeability fine-grained strata, thereby enhancing upward migration of fluid. Sandstone intrusions form when fractures and faults are propped open by naturally-injected fluidised sand (Vigorito and Hurst, 2010; Palladino et al., 2018), they persist through geologic time and once formed do not require pore-fluid overpressure to sustain dilation, thus facilitating fluid migration (Jenkins, 1930; Hurst et al., 2003; Jonk et al., 2005).

Examination of outcrops from the Panoche Giant Injection Complex (PGIC) (Vigorito and Hurst, 2010; Hurst and Vigorito, 2017) indicates that sand-propped hydraulic fractures including sills and dikes are clearly visible and their azimuth, aperture and length can be quantified (Vetel and Cartwright, 2009; Vigorito and Hurst, 2010). To investigate how different sandstone intrusion geometries are seismically imaged we create geological templates of the outcrop data to forward model 2D seismic images (Lecomte et al., 2015). Specifically, we quantify the proportion of intrusions that are resolved or detected thus allowing an estimate of sandstone intrusions captured in seismic images and the potential effect this has on fluid migration, and evaluation of fluid migration.

Since the serendipitous discovery of commercial quantities of hydrocarbons in sandstone intrusions (Jenssen et al., 1993) knowledge of sand injection complexes has grown. Ultimately this led to the deliberate exploration of analogous features for hydrocarbons (De Boer et al., 2007; Szarawarska et al., 2010) a process by which mapping of bedding-discordant sandstone intrusions became routine (Briedis et al., 2007; Schwab et al., 2014). Borehole core allowed the identification and characterisation of distinctive sedimentary facies formed during sand injection and provided a basis for enhancing the understanding of the processes by which sand is fluidised and injected (Duranti and Hurst, 2004; Vigorito and Hurst, 2010). Outcrop studies of giant sand injection complexes demonstrate that sandstone intrusions emanate from parent depositional sandstone and form highly porous and permeable conduits for fluid migration over areas of 100’s to 1,000’s km^2 and dissect 100’s m of fine-grained host strata (Vigorito and Hurst, 2010; Hurst and Vigorito, 2017). Within a spectrum of geological features that act as fluid migration pathways through the shallow portion of the crust, sand injection complexes constitute a class of seal bypass structures that remain elusive to subsurface imaging technology (Huuse et al., 2010). Discordance to bedding is one of the main characteristics of sandstone intrusions. When the discordances are at a low (<45º) angle to bedding, they are distinctive on seismic data (Jenssen et al., 1993; Lonergan et al., 2000; Huuse et al., 2004).

When sandstone intrusions are at the limit of seismic resolution and, or, steep it is very challenging to detect individual intrusions and almost impossible to resolve them (Huuse et al., 2007; Lecomte et al., 2016). High-quality outcrops of giant sand injection complexes thus provide crucial analogue data when characterising distribution and connectivity of subsurface sandstone intrusions, which are critical parameters in geological exploration, and in the evaluation of fluid and gas storage and geological waste disposal.

2. Panoche Giant Injection Complex (PGIC) and Subsurface Injection Complexes

The Panoche Giant Injection Complex (PGIC) is one of two adjacent exceptionally well-exposed sand injection complexes in the San Joaquin Valley of central California (Vigorito et al., 2008), which hosts the largest-known exposures of sand injection complexes. Outcrop of the PGIC covers almost 400 km^2 (**Fig. 1**) and examination of borehole data from the neighbouring San Joaquin Valley extends the known area to >1500 km^2 (Mario Vigorito, personal communication). There is no evidence that the PGIC was ever heated above approximately 50 ºC (equivalent to <2 km burial) and until the mid/late Eocene, it remained within a few 100's m of the Earth's surface (Hurst et al., 2017). Moreno Formation strata that host the PGIC are slightly consolidated apart from occasional carbonate concretions. Because of the large scale of PGIC outcrop, many laterally extensive, km-scale sandstone intrusions are exposed which have very similar geometry, size and thickness to subsurface examples (**Fig. 2**; Hurst and Vigorito, 2017). Here we use a >2 km long cliff section from Right Angle Canyon (RAC) (**Fig. 1c**) as our analogue for subsurface seismically resolvable sandstone intrusions. The sandstone intrusions in RAC, and generally in the PGIC (**Figs 1b** and **1c**), formed by fluidisation and injection of sand predominantly from turbiditic sandstone units in the Dosados Member (Moreno Formation) (**Fig. 1d**; Vigorito and Hurst, 2010), an interpretation that is sustained for the PGIC by mineral-chemical analysis (Hurst et al., 2017).

The PGIC sand injection complex has a well-defined architectural pattern in which intrusion geometry records the evolution of pore-fluid pressure during injection (Vigorito and Hurst, 2010; Hurst et al., 2011), and is subdivided vertically into: a lower dike zone, a sill zone and an upper dike zone. Except where eroded, the uppermost dikes of the upper dike zone terminate at the paleo-seafloor, which in many areas was the site of sand extrusion at the time of sand injection and elsewhere supported cold-carbonate seep communities (Schwartz et al., 2003; Vigorito et al., 2008; Vigorito and Hurst, 2010; Blouet et al., 2017). Very occasionally, meter-scale thick sills formed 20 to 30 meters below the paleo-seafloor. In the study area, the lower dike zone is poorly exposed and comprises only a few steep dikes, and for simplicity we model only the sandstone intrusions of the sill zone and upper dike zone. At a kilometric scale the thickest sandstone intrusions in RAC display a saucer-shaped geometry (Hurst and Vigorito, 2017) in which it is possible to differentiate a main southern and northern inner sill, a northern and southern "wing" (*sensu* Huuse et al., 2004), an outer sill and central nested intrusions (**Fig. 3**).

Subsurface examples of sand injection complexes are characterised by saucer-shaped intrusions, some of which form entire oilfields (**Fig. 2a**), and which occur in several stratigraphic intervals in restricted areas but also in disparate areas (Huuse et al., 2004; Huuse et al., 2007). To evaluate the utility of the RAC outcrop data as a subsurface analogue, comparison is made with seismic and borehole data from Volund oilfield (**Fig. 2b**), which include several generations of high-quality marine seismic reflection data and excellent borehole core data. Using synthetic seismic models of outcrops, this investigation evaluates their relevance to subsurface interpretation of sand injection complexes by comparison with Volund field.

3. Methods and field analogue dataset

Our approach to generating 2D synthetic seismic profiles from 2D geological templates follows the method of Lecomte et al. (2016) based on a 2D convolution and a point-spread function (Lecomte, 2008). An accurate 2D geometric model of the outcrop data, uploaded with Vp, Vs and density data obtained from Blue Agave #1 and N24/9-7a well log data (see below), forms the geological template - the *a priori* solution - that is required for seismic forward modeling. The outcrop analogue includes cm- to m- scale detail to avoid subjective simplification of input data prior to modeling, and are of higher resolution than the results of the seismic forward model.

Little of the fine-scale (sub-seismic) geological detail from the outcrop description is expected to be captured in the seismic forward models, but by including sub-seismic detail in models we ensure that their possible summative diffractive and back-scattered effects are not neglected (Zavalishin, 2000). At the outset, it is known that steep-angle to bedding and narrow aperture intrusions are very unlikely to be resolved and unlikely to be detected (Huuse et al., 2007). However, their effect on seismic data may produce characteristics unlike the actual sandstone geometry but may form characteristic pattern from which their presence can be inferred. Moreover, the knowledge of the *a priori* geological interpretations allows discussion of the results of the seismic forward models in unprecedented detail (Lecomte et al., 2016).

3.1. Outcrop data: the saucer-shaped intrusion, Right Angle Canyon

The eastern face of the canyon is close to a strike section approximately parallel to the underlying Dosados Member turbiditic channel, with strata dipping at ~35º NE along a slope with a 30 to 35º face (**Fig. 3**). Photogrammetric data were acquired and calibrated with logs of stratigraphic sections that were acquired across the outcrop. The sill zone is more than 150 m thick and shows clearly that dikes connect the Dosados Member sandstone unit with the saucer-shaped intrusion (**Fig. 3b**), and were the preferential pathways for the upward flow of fluidised sand. Sills intersect with underlying and lateral dikes and sill margins are, to varying degrees, discordant with bedding. Sill thickness ranges from a few centimetres up to several meters, while individual sill segments are of the order of a few hundred of meters long. Sills have steps, changes of inclination and bifurcation. The saucer-shaped intrusion is a composite feature with a central area dominated by low-angle to bedding sills that laterally steepen to form wings inclined at between 20 and 85º (**Fig. 3**). The upper dike zone is characterized by isolated dikes and dike swarms (**Fig. 3b**) in which dikes are fed both by sills or dikes that are directly connected to parent units. Dike aperture ranges from a few centimetres up to 7 meters and their length ranges from a few centimetres up to several hundred meters. Dikes often decrease in aperture upward and appear to be semi-continuous in 2D where jogs occur (Vétel and Cartwright, 2010). After correction for the regional tectonic tilt, dikes have a NNW-SSE strike orientation with dip angles to bedding ranging from a few tens of degrees up to 90°.

The northern part of the saucer-shaped intrusion has an inner sill *ca*. 7 m thick that runs along the upper part of the sill zone for about 550 m (**Fig. 3**), partly exploiting the discontinuity between mudstone and a depositional sandstone, but without causing a significant fluidization of the latter (**Fig. 3b**). At the northernmost part of the saucer the geometry is a high-angle (~73º) intrusion that defines a wing geometry. The wing is laterally continuous with aperture ranging from 2 m to 10 m, cross-cutting the stratigraphy for *ca*. 130 m, and with the dip increasing gradually from the lower to the upper part of the wing where it is almost vertical (**Fig. 3b**). The upper limit of the wing is the point where the high-angle intrusion forms an outer sill, which propagates and bifurcates northward. In the central part of the saucer the sill changes dip to form a low-angle dike, the main feeder dike, which is linked directly to the underlying parent unit (**Fig. 3b**). Also in the central area, stacked nested intrusions occur (**Fig. 3b**), which consist of low-angle intrusions that sometimes terminate against high-angle dikes or simply pinch out away from their mid-point.

The southern part of the saucer has an inner sill, which is up to 13 m thick, 470 m long and located in the upper part of the sill zone (**Fig. 3b**). To the north and south of the thickest section the inner sill thins gradually to 5 m and 8 m, respectively. Near its thickest point the sill steps up to the south. A composite wing is formed by a rapid increase in steepness up to approximately 85º, which then bifurcates into a series of offset dikes with similar orientation

(**Fig. 3b**). In the lower part of the wing the dikes diverge but merge upward and then bifurcate into lower aperture dikes. The cumulative thickness of the dikes in the lower and upper parts of the wing is *ca.* 10 m and *ca.* 6 m, respectively. The excellent and extensive exposure reveals a plethora of features similar to those recognised in core (Duranti et al., 2002; Duranti and Hurst, 2004; Hurst et al., 2011) and seismic data (Huuse et al., 2004; Huuse et al., 2007) from subsurface sand injection complexes, which is why the PGIC is the prime outcrop analogue for understanding subsurface sand injection complexes.

3.2. Petrophysical data

When creating seismic models of outcrops as analogues for subsurface interpretation, models need to be populated by accurate petrophysical data. Petrophysical characteristics of outcrops are modified by uplift and weathering so to avoid compromising the subsurface (seismic) model, the RAC template uses data from the same stratigraphic interval in the Blue Agave #1 borehole located 11 km NE of RAC (**Fig**. **1b**). The Moreno Formation in Blue Agave #1 is at a similar depth to the reservoir interval in Volund field (Schwab et al., 2014).

Blue Agave #1 borehole (Cheney Ranch gas field - San Joaquin Valley)

The entire Moreno Formation (McGuire, 1988) is penetrated in Blue Agave #1, and a full suite of wireline log data are available (https://maps.conservation.ca.gov/doggr/wellfinder/#close). This facilitates correlation between Blue Agave #1 and the RAC section (**Figs 1c** and **4**). In Blue Agave #1 the top and base of the Moreno Formation occur at 1672 m and 2250 m subsurface, respectively. Wireline log data show variations in bulk density and pressure-wave velocity (V_p) which correspond to lithological variations (mudstone, sandstone and diagenetic carbonate concretions). Shear-wave velocity (V_s) was derived from V_p using the Greenberg-Castagna equation (Greenberg and Castagna, 1992) (see **Fig. 4**). Top surfaces of the biosiliceous mudstone of the Marca Member, the sandstone-rich slope-turbiditic deposits of the Tierra

Loma Member and the sandstone of the Dosados Member are important features that are identified in the borehole and outcrop and are correlated with confidence (**Fig. 4**).

N24/9-7A borehole (Volund oil field - Norwegian North Sea)

Because the Blue Agave #1 wireline data do not allow a clear identification of the sandstone intrusions, wireline data from the N24/9-7A borehole, Volund oilfield (De Boer et al., 2007; Schwab et al., 2014) were used to provide petrophysical data for intrusions in the seismic forward modeling. The Volund reservoir is entirely formed by saucer-shaped sandstone intrusions (**Fig. 2b**; Huuse et al., 2004; Schwab et al., 2014). Borehole N24/9-7A penetrates the saucer-shaped intrusion at ~1900 m subsea, which approximates to the position of the sandstone intrusions in Blue Agave #1. Coincidence of the burial depths and the presence of similar lithologies allows us to infer similar lithostatic overburden in both boreholes and justifies the use of the N24/9-7A data from sandstone intrusions in the seismic forward models. V_p and bulk density of the sandstone intrusions are lower than those of the host mudstone. Borehole geophysical data from the Volund field are publically available (http://factpages.npd.no/factpages/default.aspx?culture=en&nav1= wellbore).

3.3. 2D geological and petrophysical model

A critical aspect of the geological model is the creation of a cross section of RAC in which the geometry of the sandstone intrusions and the geometry of the surrounding host strata are depicted accurately (**Fig. 5a**). Stratigraphic logs, dip/strike measurements, photogrammetric data and geo-referenced satellite images, are integrated in the model. The main dike orientation is approximately perpendicular to the 2D cross section (**Fig. 5b**), thus the dip angles are similar to the true inclinations of the sandstone intrusions. Because the Moreno Formation and the host strata in well N24/9-7A are unlikely to have identical petrophysical characterisitcs, using petrophysical data from Blue Agave #1 (**Fig. 4**), including Vp, V_s and interval bulk density (**Table 1**), ensures that the seismic model of the RAC contains accurate geometry and petrophysical data. Using subsurface data from well N24/9-

7A may introduce petrophysical characteristics uncommon to the Moreno Formation, for example, a lack of strong acoustic impedance may compromise imaging of diagnostic features of sand injection complexes such as the jack-up of host strata (Szarawarska et al., 2010) and will generally fail to resolve the geological features present in the outcrop based models. Our seismic model of RAC is a base case unique to the Moreno Formation that allows meaningful comparison to subsurface seismic data, herein specifically Volund field.

3.4. Geophysical method (2D convolution)

Modeling uses ray-based point-spread functions (PSF) to produce a synthetic seismic reflection section by convolution of an input 2D reflectivity model (Lecomte et al., 2003; Lecomte et al., 2016). PSF create elementary images of pre-stack depth migration. The method advances beyond 1D convolution by implicitly adding a complete resolution pattern, unrestricted to a single direction, and incorporating illumination effects (Lecomte et al., 2016). Thereby, extended convolution makes use of a given velocity model for the overburden and of a seismic survey geometry, thus having both resolution and illumination patterns controlled by actual wave propagation effects. The synthetic seismic images that are produced correspond to ideal results of PSDM imaging, the latter being a necessity when modeling complex geology (Gray et al., 2001) such as sand injection complexes.

The overburden model and survey geometry used in the seismic forward modeling are shown (**Fig. 5c**) with the corresponding PSF placed in the corner of each synthetic seismic section (**Fig. 5d**). When interpreting a seismic image, one must keep in mind that any 2D reflectivity “scatterer” in the input model consequently appears as the PSF with its corresponding polarity and strength. Complex 2D interference between all the PSF footprints combine to form the final image. As will be illustrated, the resolution pattern obtained for the model in figure **5d** results in a PSF with a central peak size of approximately a quarter wavelength vertically and a half wavelength horizontally, these being typical dimensions for a good quality seismic acquisition and imaging (Simm and Bacon, 2014). Within the acquisition and migration (Kirchhoff PSDM) conditions of this experiment the illumination is limited to ~45° in dip as geological dips steeper than this are not imaged (Biondi, 2001).

Similarity between the 2D geometry of saucer-shaped intrusions in Volund field and RAC (**Fig. 2b**) are indicative that the latter is a suitable analogue for forward seismic simulation of the outcrop data (**Fig. 5a**). The dominant frequencies of the full-stack seismic volume of Volund are between 30 and 40 Hz (Szarawarska et al., 2010). Accordingly, the same range of frequencies were used in the seismic forward models. Although a wavelet directly extracted from Volund field data could be used for the modeling, simple zero-phase Ricker wavelets were used with peak frequencies of 30 and 40 Hz for convolution of the 2D reflectivity model. This avoided possible artefacts such as high secondary lobes with, *e. g.*, Ormsby wavelets (Ryan, 1994).

4. Results

4.1. *Synthetic seismic models of sandstone intrusions*

The 30 Hz seismic forward model of the RAC saucer-shaped sandstone intrusion has well-defined horizontal seismic reflections (**Fig. 5d**). These reflectors are related to acoustic impedance contrasts between mudstone units, between mudstone and depositional sandstone or where (close to) bedding-parallel sandstone intrusions (sills) occur. Sub-horizontal and high-angle seismic reflections cut across the horizontal reflections and are associated with the presence of sandstone dikes (compare **Figs 5a** and **5d**). Thick sub-horizontal intrusions that form the inner sill are well illuminated (**Fig. 5d**) although the peak to trough interval in most cases is dissimilar to the actual thickness of intrusions.

The discrepancy between the distance from peak to trough and the true thickness is controlled by the frequency of the impulses and the interference effects between stratigraphic reflections and reflections generated along sandstone intrusion contacts (**Fig. 6**).

4.1.1 *Stepped seismic reflections related to the occurrence of wedge geometry*

Using the 40 Hz seismic forward model to image the northern wing demonstrates how the geometric relationship between the stepped intrusion and host strata (**Figs 6a** and **6b**) creates a complex wedge-geometry cluster. The sandstone intrusion cuts strata that have contrasting acoustic impedance (**Fig. 6c**). The effects of constructive and destructive interference (Widess, 1973) on the wavelet amplitude are revealed (**Figs 6c** and **6d**, left hand insets). In the case of constructive interference, the wedge-geometry causes amplitude enhancement of the seismic signal, whereas destructive interference either attenuates or cancels the seismic signal (**Figs 6c** and **6d**). In the latter case discontinuities along seismic reflections produce artefact steps (tuning wedge steps) whereas in reality the sandstone intrusion is laterally continuous (**Fig. 6d**).

4.1.2 *Stepped seismic reflections and discordant amplitudes related to the presence of high-angle sandstone intrusions*

Seismic detection of dikes depends on factors such as their thickness, contrast in acoustic impedance and dip angle, with high-angle to bedding dip the main detrimental factor influencing the detection of intrusions (Biondi, 2001). With this in mind, examples are evaluated that show how variations of dip angle of sandstone intrusions produce discordant amplitude anomalies or the complete absence of seismic response.

The maximum dip angle that is illuminated using the seismic survey array (**Fig. 5c**) is ~45° (**Fig. 5d**, top right-hand insets). Above this value reflections of seismic rays along dike margins are likely to be undetected (**Fig. 5d**). Where the margins of sandstone intrusions dip at angles greater than ~45° they produce artefact discontinuities along the seismic reflections. Results of the forward modeling reinforce the concept (**Figs 6c** and **6d**) and indicate that the steps highlighted at point 1 are undoubtedly imaging artefacts.

Examples of high-angle sandstone intrusions from the southern part of RAC (**Fig. 7**) reveal that the composite wing consists of several steep-to-bedding offset intrusions (**Figs 7b** and **7c**), which because of high dip-angles (average dip ~75°) is only partially detected (**Fig. 7d**). Moreover, in this area the reflection of the seismic rays highlights the presence of a seismic amplitude anomaly, but does not provide accurate information about the geometry of the sandstone intrusions (compare **Figs 7c** and **7d**). Clues about the presence of sandstone intrusions are obtained from observation of the relationship between the inner sill and the jack-up (**Figs 7c** and **7d**); jack-up describes the uplift of the overburden above sandstone intrusions relative to areas without intrusions. Jack-up of the base of Marca Member overlies both the southern wing and part of the southern inner sill (**Figs 7a** and **7b**) and is highlighted by the displacement of bedding parallel seismic reflections (compare **Fig. 7b** and **7c**). These coincide exactly with the location of the seismic amplitude anomalies caused by the complex geometry of the composite wing. In this case the jack-up is directly indicative of the presence of sandstone intrusion.

Well-defined discordant amplitude anomalies are present where large aperture (>4m) dikes dip with angles of less than ~45° (point 1 in **Fig. 7c**). Again, when the dip angle of intrusions exceeds the maximum dip angle that is illuminated (point 2 in **Figs 6c** and **7c**) no amplitude anomalies are recorded, which limits the possibility of detecting sandstone intrusions.

4.2. Synthetic vs actual data

Comparison of the 40 Hz forward model of RAC with actual seismic data from Volund oilfield highlights remarkable similarities (**Fig. 8**). The synthetic data and Volund oilfield data are of comparable lateral and vertical scale, and in terms of geometry and architecture they are almost identical. In both the seismic sections the main sandstone intrusions consist of: 1) an inner sill; 2) two main bedding-discordant amplitude anomalies (wings); 3) the jack-up of the horizontal reflections approximately above and parallel to the location of the inner sill

(**Fig. 8**). Detail from the Volund seismic data (**Fig. 8a**) shows clear stepped seismic reflections along the inner sill which, in the light of the forward modeling may be interpreted either as high-angle intrusion steps or tuning wedge steps (compare **Fig. 8a** and **8b**). Where horizontal stratigraphic reflections intersect high-angle seismic reflections the effect of tuning-wedge amplitude enhancement is generated, in which case the increase of signal amplitude could be misinterpreted as a variation in target acoustic impedance, which is incorrect. Comparison between the cross-sectional geometry of Volund field and RAC reveals similar overall geometry although Volund has thicker sandstone intrusions (**Fig. 8c** and **8d**). The geological model has vastly more dikes than resolved in either seismic interpretation (compare **Fig. 8d** and **8e**).

4.3. *Detection vs resolution*

The limit of vertical resolution is a quarter wavelength (λ/4) of the dominant frequency of the seismic source.

When the thickness of a layer is greater than the limit of vertical resolution, reflections at its top and base begin to resolve as separate events. Below the limit of vertical resolution, constructive or destructive interference of waves from closely-spaced reflections depending on their relative impedance contrasts. These contrasts control the final imaging. Wave interference limits the possibility to discriminate the actual thickness of a bed but not the possibility to detect its thickness as the combined reflection amplitude should be linearly related to its thickness below λ/8 (Shoemaker et al., 2007).

For actual data, the limit of detectability depends on the acoustic impedance contrast, the wavelet spectrum and the signal-to-noise ratio of the seismic (Zhang and Castagna, 2011). Thus, a thin bed cannot be resolved if its seismic amplitude merges with the background noise (Simm and Bacon, 2014). The limit of detectability of thin-bedded hydrocarbon-saturated sandstone, characterized by strong contrast in acoustic impedance with the surrounding strata, is usually set between $\lambda/20$ and $\lambda/30$ (Widess, 1973; Sheriff and Geldart, 1995; Zhang and Castagna, 2011). To gain insight into the proportion of bedding-discordant intrusions (dikes) that would not be detected during a seismic survey we compiled measurements of strike, dip and thickness of dikes (**Fig. 9**).

Because the limit of detectability of sandstone intrusions also depends on the ability to illuminate their dip angle (Vermeer, 2012), using detailed outcrop data and a defined survey design in a seismic forward model allows the quantification of the percentage of dikes that are likely to be resolved or detected in the subsurface. Differentiate very-low angle dikes from sills may be challenging, therefore only dikes with a dip angle above 10° with respect to bedding and >5 cm thick were included. Thinner dikes would never be detected individually, regardless of their dip angle.

Taking into account that seismic methods have limited detection-ability of sandstone intrusions above 45°, only 22% of the dikes known to be present are likely to be detected (**Fig. 9a**), while the remaining 78% fall in the undetectable field (steeper than 45°) (**Fig. 9a**). If dike thickness and dip angle are known the percentage of sandstone intrusions that are detectable can be calculated by assuming that the peak frequency of the pulse (*f*) and the velocity of the compressional waves (V_p) at the zone of interest are constrained. When fields of resolvable, detectable and undetectable - for a dominant frequency of 40 *Hz*, V_p of 2000 *m/s* and a maximum dip angle illuminated of 45° - are calculated (**Fig. 9b**), it is clear that most dikes are undetectable; approximately 10% of the sandstone intrusions are detectable and <1% are resolved with reasonable accuracy (**Fig. 9b**). Changing the values of frequency and wave velocity shift the limits of the detectable and undetectable fields. The data show that the proportion of thick dikes (range between 1.6 to 13 m) decreases as the dip angle of intrusions increases (**Fig. 9c**). However, despite most dikes having high dip-angles, most of the sandstone volume is accommodated in the thick (wide aperture) low-angle intrusions (**Fig. 9c**), which represent most of the sandstone volume associated with the wings of a saucer-shaped intrusion. Unsurprisingly, the resolution of the geometry of individual parts of the sandstone intrusion is more tenuous than resolving the overall geometry. Consequently, saucers and sills generally appear more discontinuous than in reality (**Figs 8d** and **8e**) and dikes are resolved as "blobs" (**Figs 7d** and **7e**).

The low probability of detecting high-angle sandstone intrusions means that seismic interpreters need to be aware of the likely underestimation of the quantity of dikes, their reservoir volume and their spatial distribution within an injection complex. The seismic-based model (**Fig. 8d**) of the 40 Hz synthetic seismic line of RAC highlights the importance of this point. Comparison of the seismic forward model and the initial geological model (**Figs 8d** and **8e**) shows that mapping of the top and the base of the thick sandstone intrusions should be straightforward, but that it is more challenging to interpret the sill zone and the upper dike zone, where sub-seismic and high angle (> 45º to bedding) sandstone intrusions occur. Computation of the volume of sandstone present in the forward model compared to reality (**Figs 8d** and **8e**) shows that between 20 and 40% of the volume of the sandstone present may be undetected in seismic images. In practice, this means that one makes a seismic interpretation of sandstone intrusion complexes significant underestimation will occur, and - more important in the context of promoting leakage in the upper dike zone - the degree of connectivity between individual sandstone intrusions will be grossly underestimated.

5. Discussion

5.1. *Comparison of seismic data from the outcrop model and Volund field*

In terms of the scale of features that are resolved on the 3D seismic data from Volund field, the overall geometry of the forward seismic model of the RAC saucer-shaped intrusion is remarkably similar (**Fig. 8**). The lateral extent and height of the intrusion indicate that the fracture systems which host both intrusions are very similar, which is indicative of a similar process of formation. In the case of RAC, the position of the paleo-seafloor, hence the depth of burial at which sand injection occurred, are constrained (*cf.* Vigorito and Hurst, 2010). This relationship is more speculative in Volund field where paleo-seafloor extrusions are not clearly visible on seismic data and probably not identified in boreholes (De Boer et al., 2007; Schwab et al., 2014). A significant difference between the intrusion complexes is the thickness of the sandstone: Volund field generally >20 m thick in the lower sill-dominated part of the saucer (**Fig. 8a**) and RAC <20m thick throughout most of the saucer (**Fig. 8b**). Despite the thickness difference, the fracture geometries have similar asymmetric geometries.

Saucer-shaped intrusions, including wings, conical intrusions and other variants in the realm of sand injectites, are well know from 3D seismic data (MacLeod, 1999; Duranti et al., 2002; Huuse et al., 2004; Huuse et al., 2007; Szarawarska et al., 2010). In stark contrast, well-exposed outcrop examples of saucer-shaped intrusions at similar scale are unusual (Surlyk et al., 2007; Vigorito and Hurst, 2010; Hurst and Vigorito, 2017). The disparity in knowledge of subsurface and outcrop data has limited the informed geological modeling of sandstone intrusions and is a significant reason why constraining the volumes of intrusive sandstones remains challenging. Because seismic data acquisition techniques fail to image dikes (steep to bedding), a significant volume of sandstone may be invisible, as illustrated in the outcrop seismic model (**Figs 8d** and **8e**). Arguably more significant is how the failure to image dikes can lead to gross underestimation of vertical transmissivity in what appear to be low permeability seals (Vigorito and Hurst, 2010). Undetected dikes (in the upper dike zone) similarly lead to underestimation of vertical hydraulic continuity in the mudstone dominated overburden. In the RAC outcrop model ~78% of dikes are undetected (**Fig. 9**), which although they are not volumetrically large, they are likely to have a strong influence on hydraulic continuity throughout a sand injection complex.

5.2. *Consequences of tuning effects*

Discordance between sandstone intrusions and finer-grained host strata causes obvious problems when interpreting seismic data where sandstone intrusions are present (Huuse et al., 2007). Intrusions steeper than 45º do not produce reflections similar to the intrusion geometry but produce features that could be interpreted as random imaging-artefacts, or are undetected **(Figs 5d, 6d** and **7d**). Tuning effects occur along wedge-shaped units that have margins inclined at less than 45º to bedding and cause both constructive and destructive interference (**Fig. 6**), which creates step geometry, apparent thickening and thinning of sandstone, and may produce a more complex external geometry than exists (**Fig. 6d**). Where intrusions steepen more than 45º, they transform from resolvable or detectable to undetectable and form images unfamiliar in the context of conventional sandstone intrusions (**Figs 7c** and **7d,** points 1 and 2). Steep composite intrusions produce unclear reflections that do not indicate the presence of sandstone and may be open to interpretation as imaging artefacts or noise possibly associated with fluid substitution, rather than sandstone intrusions **(Fig. 5d,** dike swarm and **Figs 7c** and **7d**, composite wing).

Limitations of resolution and detection may hinder the accurate estimation of sandstone volume and geometry, which affects connectivity, thus compromising the spatial representation of the distribution of sandstone (MacLeod et al., 1999; Duranti et al., 2002; Schwab et al., 2014) (**Figs 5, 6** and **7**). Where a dike swarm up to ~100m across and >200m high with individual dikes of 0.5 to >3 m aperture occurs, seismic images do not capture realistically the sandstone geometry or distribution (**Figs 5d** and **7**). Within the area of the dike swarm the forward model creates small discordances among flat-lying reflections and some low-relief folds along the top of the Marca Member (**Fig. 5d**). All of these effects are tuning artefacts caused by high-angle intersections between sandstone dikes and none of them represent geological features present at outcrop. It seems likely that when interpreting the possible presence of sandstone dikes in the upper dike zone one should expect seismic images to have unrealistic geological features rather than linear, dike-like, geometry.

5.3. *Bedding-discordant amplitude anomalies in different geological context*

Mass-transport deposits are generally associated with chaotic seismic facies, which are seen as the seismic expression of intensely folded strata, imbricated strata and slide-scar surfaces (Kneller et al., 2016). They produce a wide range of bedding-discordant amplitude anomalies (Bull et al., 2009) similar to those present in sand injection complexes. Bedding-discordance may be misinterpreted if tuning-wedge step effects or tuning-wedge amplitude enhancement effects are not taken into account. In common with sandstone intrusions, seismic forward models of mass-transport deposits fail to detect surfaces characterized by high dip angles (Dykstra et al., 2011).

5.4. *Fluid flux and seafloor seepage*

Sandstone dikes are conduits for fluid flow to the surface, expelling sand and fluid during their emplacement (Hurst et al., 2011) and subsequently enhancing longer-term drainage from deeper strata (Schwartz et al., 2003; Mazzini et al., 2003; Blouet et al., 2017). Because dikes propagate at lower pore-fluid pressure than sills (Hurst et al., 2011), in a sand injection complex where pore-fluid pressure was sublithostatic and the underlying pressure cell restricted in volume, dikes may form the only sandstone intrusions present. Dikes would of course emanate from parent units and, as observed in the PGIC, they may propagate through 100's meters of host strata and reach the paleo-seafloor (Vigorito et al., 2008; Hurst et al., 2011). It is unlikely that any dikes are detectable (**Fig. 9**), and even if they occur as dike swarms the seismic images are likely to form features that do not resemble dike geometry (**Figs 5a** and **5d**). Areas of sand injection complexes where sills and saucers are absent, but dikes occur, appear similar to host strata in which no intrusions are present. The upper dike zone is difficult to image on actual seismic data (**Fig. 8a**) and in seismic forward models (**Figs 5d** and **8b**), which has direct implications on the estimation of rates and volumes of fluid expelled from otherwise low permeability host strata that in turn relate directly to estimates of their porosity loss (Hurst et al., 2012).

6. Conclusions

Seismic forward modeling of large outcrops confirms the tacit assumption that seismic images fail to image many geometric features of sandstone intrusions. Seismic models of kilometre-scale saucer-shaped intrusions from the Panoche Giant Injection Complex create cross-sectional profiles that have very similar geometry and dimensions to sandstone intrusions from the Volund oilfield. Almost 78% of dikes in the outcrop model are likely to be undetected. Generally, thin and steep intrusions are not seismically imaged but were explicitly included in the seismic modeling. Inevitably, hydraulic continuity in subsurface models of sand injection complexes is underestimated.

Results of seismic modeling of outcrop show that even high seismic frequency (40 Hz) fails to detect most steep (>45º to bedding) intrusions. Individual steep dikes are undetected. Intrusions <45º to bedding are routinely detected but their thickness is rarely resolved and their geometry may not resemble genuine. Dike swarms are detected but the seismic images do not resemble at the actual geometry, rather, a group of minor bedding discordances, including small folds. Similar artefact geometry may be representative of seismic images of dikes on subsurface seismic data. Lack of detection of dikes gives misleading impressions of vertical transmissibility in the overburden (upper dike zone) of sand injection complexes.

Up to the 40% of the total sandstone volume in an injection complex may be not imaged in actual seismic data, which creates significant uncertainty related to estimation of sandstone storativity. If unrecognised, underestimation of vertical and horizontal transmissivity is implicit in otherwise low permeability (mudstone) strata in which the only intrusions are dikes. Sandstone dikes are conduits for fluid escape during burial, but because *ca*. 78% are undetected, underestimation of fluid flux will ensue.

Where there is discordance between lithologies with contrasting amplitude impedance, which is a characteristic of sandstone intrusions, tuning wedge-effects occur, such as tuning wedge steps and tuning wedge amplitude enhancement. Seismic modeling demonstrates that constructive and destructive amplitude interference generates imaging artefacts that produce incorrect images of sandstone intrusion thickness. Recognition of the significance of tuning wedge-effects enables the use of seismic models of outcrops to derive more accurate descriptions when undertaking subsurface data interpretation. Failure to recognise possible artefacts caused by constructive and destructive amplitude interference causes erroneous seismic interpretation.

The immediate implications of this work herein include petroleum and groundwater exploration and production, and evaluation of top seal integrity analysis for carbon and nuclear waste storage.

Acknowledgments

We acknowledge the support of sponsoring companies of Phase 3 of the Sand Injection Research Group (SIRG). The Norwegian Petroleum Directorate (NPD) are thanked for providing seismic data from Volund oil field. Also, we wish to acknowledge NORSAR Innovation AS for providing the academic licence for the SeisRoX software and the California Bureau of Land Management for facilitating access to the outcrop area.

References

Biondi, B., 2001. Kirchhoff imaging beyond aliasing. Geophysics, v. 66, pp. 654–666.

Blackford, J., Stahl, H., Bull, J. M, et al., 2014. Detection and impacts of leakage from sub-seafloor deep geological Carbon Dioxide Storage. Nature Climate Change, v. 4, pp. 1011-1016.

Blouet, J.-P., Imbert P., Fouber A., 2017. Mechanisms of biogenic gas migration revealed by seep carbonate paragenesis, Panoche Hills, California. AAPG Bulletin, v. 101, no. 8, pp. 1309-1340, doi:10.1306/10171616021.

Braccini E., de Boer W., Hurst A., Huuse M., Vigorito M., Templeton G., 2006. Sand injectites. Geology, v. 186 (1-2), pp. 67-88.

Briedis, N. A., Bergslien, D., Hjellbakk, A., Hill, R. E., Moir, G. J., 2007. Recognition criteria, significance to field performance, and reservoir modeling of sand injections in the Balder field, North Sea. In: Hurst A., and Cartwright J. A., eds., Sand injectites: Implications for hydrocarbon exploration and production: AAPG Memoir 87, pp. 91–102.

Bull, S., Cartwright, J., Huuse, M., 2009. A review of kinematic indicators from mass-transport complexes using 3D seismic data. Marine and Petroleum Geology, v. 26, pp. 1132–1151, doi.org/10.1016/j.marpetgeo.2008.09.011.

Cartwright, J., Aplin, A., Huuse, M., 2007. Seal bypass systems. AAPG Bulletin, v. 91, pp. 1141-1166, doi:10.1306/04090705181.

Cevatoglu, M., Bull, J. M, Vardy, M.E., Gernon, T.M., Wright, I.C., Long, D., 2015. Gas migration pathways, controlling mechanisms and changes in sediment acoustic properties observed in a controlled sub-seabed CO2 release experiment. International Journal of Greenhouse Gas Control, v. 38, pp. 26-43.

De Boer, W., Rawlinson, P. B., Hurst, A., 2007. Successful exploration of a sand injectite complex: Hamsum prospect, Norway Block 24/9. In: Hurst A., and Cartwright J. A., eds., Sand injectites: Implications for hydrocarbon exploration and production: AAPG Memoir 87, pp. 65–68.

Duranti, D., Hurst, A., Bell, C., Groves, S., Hanson, R., 2002. Injected and remobilised Eocene sandstones from the Alba Field, UKCS: core and wireline characteristics. Petroleum Geoscience, v. 8, pp. 99–107.

Duranti, D., Hurst, A., 2004. Fluidisation and injection in the deep-water sandstones of the Eocene Alba Formation (UK North Sea). Sedimentology, v. 51, pp. 503–531.

Dykstra, M., Garyfalou K., Kertznus V., Kneller B. C., Milana J. P., Molinaro M., Szuman M., Thompson P., 2011. In: H. Posamentier, P. Weimer, and C. Shipp, eds., Mass-transport deposits: Combining outcrop studies and seismic forward modeling to understand lithofacies distributions, deformation, and their seismic expression: SEPM Special Publication 95, pp. 293–310.

Gray, S. H., Etgen J., Dellinger J., Whitmore D., 2001. Seismic migration problems and solutions. Geophysics, v. 66, pp. 1622–1640, doi: 10.1190/1.1487107.

Greenberg, M. L., Castagna J. P., 1992. Shear-wave velocity estimation in porous rocks: Theoretical formulation, preliminary verification and applications. Geophysical Prospecting, v. 40, pp. 195–209, doi: 10.1111/j.1365-2478.1992.tb00371.x.

Hurst, A., Cartwright, J.A., Huuse, M., Jonk, R., Schwab, A.M., Duranti, D., Cronin, B.T., 2003. Significance of large-scale sand injectites as long-term fluid conduits: evidence from seismic data. Geofluids, v. 3, 263-274.

Hurst, A., Scott, A., Vigorito, M., 2011. Physical characteristics of sand injectites. Earth-Science Reviews, v. 106, pp. 215–246.

Hurst, A., Vigorito, M., Scott, A., Stanzione O., 2012. Sand Injectites - Implications for Overpressure and Compaction. 74th EAGE Conference & Exhibition incorporating SPE EUROPEC 2012 Copenhagen, Denmark, 4-7 June 2012.

Hurst A., Vigorito M., 2017. Saucer-shaped sandstone intrusions: An underplayed reservoir target. AAPG Bulletin, v. 101, no. 4 (April 2017), pp. 625-633, doi.org/10.1306/011817DIG17070.

Hurst A., Morton A., Scott A., Vigorito M., Frei D., 2017. Heavy-mineral assemblages in sandstone intrusions: Panoche giant injection complex, California, U.S.A. Journal of Sedimentary Research, v. 87, pp. 388-405, doi.org/10.2110/jsr.2017.22.

Huuse, M., Duranti, D., Steinsland, N., Guargena, C. G., Prat, P., Holm, K., Cartwright, J. A., Hurst, A., 2004. Seismic characteristics of largescale sandstone intrusions in the Paleogene of the South Viking Graben, UK and Norwegian North Sea. In R. J. Davies, J. Cartwright, S. A. Stewart, J. R. Underhill, M. Lappin, eds., 3D seismic technology: application to the exploration of sedimentary basins. Geological Society, London Memoir, v. 29, pp. 257–271.

Huuse, M. J., Cartwright, J. A., Hurst, A., Steinsland, N., 2007. Seismic characterization of large-scale sandstone intrusions. In: Hurst, A., Cartwright, J., eds., Sand Injectites: Implications for Hydrocarbon Exploration and Production: AAPG Memoir, Tulsa, pp. 21–35.

Huuse M., Jackson C. A. L., Van Rensbergen P., Davies R. J., Flemings P. B., Dixon R. J., 2010. Subsurface sediment remobilization and fluid flow in sedimentary basins: an overview. Basin Research, v. 22, pp. 342-360, doi: 10.1111/j.1365-2117.2010.00488.x.

Jenkins, O. P., 1930. Sandstone dikes as conduits for oil migration through shales. AAPG Bulletin, v. 14, pp. 411-421.

Jenssen, A. I., Bergslien, D., Rye-Larsen, M., Lindholm, R. M., 1993. Origin of complex mound geometry of Paleocene submarine-fan reservoirs, Balder Field, Norway. In J. R. Parker, eds., (pp. 135–143). Petroleum Geology of Northwest Europe: Proceedings of the 4th Conference, London: Geological Society.

Jonk, R., Parnell, J., Hurst, A., 2005. Aqueous and petroleum fluid flow associated with sand injectites. Basin Research, v. 17, pp. 241-257.

Karstens J., Berndt C., 2015. Seismic chimneys in the Southern Viking Graben – Implications for palaeo fluid migration and overpressure evolution. Earth and Planetary Science Letters, v. 412, pp. 88-100.

Kneller, B., Dykstra, M., Fairweather, L., Milana, J.P., 2016. Mass-transport and slope accommodation: implications for turbidite sandstone reservoirs. AAPG Bulletin, v. 100, pp. 213–235, doi.org/10.1306/09011514210.

Lecomte, I., Gjøystdal, H., Drottning, Å., 2003. Simulated Prestack Local Imaging: a robust and efficient interpretation tool to control illumination, resolution, and time-lapse properties of reservoirs, Expanded Abstracts, SEG 73nd Annual Meeting, Dallas.

Lecomte, I., 2008. Resolution and illumination analyses in PSDM: A ray-based approach. The Leading Edge, v. 27, pp. 650-663.

Lecomte, I., Lavadera, P. L., Anell, I., Buckley, S. J., Schmid, D. W., Heeremans, M., 2015. Ray-based seismic modelling of geological models: understanding and analyzing seismic images efficiently. Interpretation, v. 3, no. 4, SAC71-SAC89, doi: 10.1190/INT-2015-0061.1.

Lecomte, I., Lavadera, P.L., et al., 2016. 2 (3) D convolution modelling of complex geological targets - beyond 1D convolution. First Break, v. 34, pp. 99–107.

Lonergan, L., Lee, N., Johnson, H. D., Cartwright, J. A., Jolly, R. J. H., 2000. Remobilization and injection in deepwater depositional systems: implications for reservoir architecture and prediction. In: Weimer, P., Slatt, R. M., Coleman, J., Rosen, N. C., Nelson, H., Bouma, A. H., Styzen, M. J., Lawrence D.T., eds., Deep-water reservoirs of the world (pp. 515–532). GCSSEPM Foundation, 20th Annual Conference, Houston.

MacLeod, M.K., Hanson, R.A., Bell, C.R., McHugo, S., 1999. The Alba field ocean bottom cable seismic survey: Impact on development. The Leading Edge, v. 18, pp. 1306–1312.

Mazzini, A., Jonk, R., Duranti, D., Parnell, J., Cronin, B., Hurst A., 2003. Fluid escape from reservoirs: Implications from cold seeps, fractures and injected sands Part I. The fluid flow system: Journal of Geochemical Exploration, v. 78–79, pp. 293–296, doi:10.1016/S0375 6742(03) 00046-3.

McGuire, D. J., 1988. Depositional framework of the Upper Cretaceous–lower Tertiary Moreno Formation, central San Joaquin Basin, California. In: Graham, S. A., eds., 1988, Studies of Geology of the San Joaquin Basin: Pacific Section S.E.P.M., v. 60, pp. 173-188.

Moser T. J., Howard, C. B., 2008. Diffraction imaging in depth. Geophysical Prospecting, v. 56, pp. 627-641.

Palladino G., Alsop G. I., Grippa A., Zvirtes G., Phillip R. P., Hurst A., 2018. Sandstone-filled normal faults: A case study from central California. Journal of Structural Geology, v. 110, pp. 86-101.

Ryan, H., 1994. Ricker, Ormsby, Klauder, Butterworth – A choice of wavelets. CSEG Recorder, v. 7, pp. 8 - 9.

Schwab, A. M., Jameson, E. W., Townsley, A., 2014. Volund Field: development of an Eocene sandstone injection complex, offshore Norway. In McKie T., Rose, P. T. S., Hartley, A. J., Jones, D. W., and Armstrong, T. L., eds., Tertiary deep-marine reservoirs of the North Sea region: Geological Society, London, Special Publications 2015, v. 403, pp. 247–260, doi: 10.1144/SP403.4.

Schwartz, H., Sample, J., Weberling, K.D., Minisini, D., Moore, J.C., 2003. An ancient linked fluid migration system: cold-seep deposits and sandstone intrusions in the Panoche Hills, California, USA. Geo-Marine Letters, v. 23, 340–350, doi:10.1007/s00367-003-0142-1.

Sheriff, R. E., Geldart, L. P., 1995. Exploration seismology (2nd Edn). Cambridge University Press (pp. 592).

Shoemaker, M. L., Robinson, J. B., Trumbly, P. N., Brennan, B. A., 2007. Prediction of thin bed reservoirs below ¼ wavelength tuning thickness using full bandwidth inverted seismic impedance. International Petroleum Technology Conference, Dubai, U.A.E., 4–6 December 2007.

Simm, R., Bacon, M., 2014. Seismic Amplitude: An Interpreter's Handbook. Cambridge University Press (pp. 271).

Szarawarska, E., Huuse, M., Hurst, A., De Boer W., Liwei L., Molyneux S., Rawlinson, P., 2010. Three-dimensional seismic characterization of large-scale sandstone intrusions in the lower Paleogene of the North Sea: Completely injected vs. in situ remobilized saucer-shaped sand bodies. Basin Research, v. 22, pp. 517–532.

Vermeer G. J. O., 2012. 3D seismic survey design (2nd Edn). Geophysical Reference Series no. 12 (pp. 342).

Vetel, W., Cartwright, J. A., 2009. Emplacement mechanics of sandstone intrusions: insights from the Panoche Giant Injectite Complex, California. Basin Research, v. 22, pp. 783–807.

Vigorito, M., Hurst, A., Cartwright, J., Scott, A., 2008. Regional-scale shallow crustal remobilization: processes and architecture. Journal of the Geological Society, London, v. 165, pp. 609–612.

Vigorito, M., Hurst, A., 2010. Regional sand injectite architecture as a record of porepressure evolution and sand redistribution in the shallow crust: insights from the Panoche Giant Injection Complex, California, Journal of the Geological Society, London, v. 167, pp. 889-904.

Zhang R., Castagna J., 2011. Seismic sparse-layer reflectivity inversion using basis pursuit decomposition. Geophysics, v. 76, pp. 147-158, doi: 10.1190/GEO2011-0103.1.

Zavalishin, B. R., 2000. Diffraction problems of 3D seismic imaging. Geophysical Prospecting, v. 48, pp. 631–645.

Widess, M.B., 1973. How thin is a thin bed? Geophysics, v. 38, pp. 1176-1180.

https://maps.conservation.ca.gov/doggr/wellfinder/#close (API: 01924225; Well Number: 1; Lease Name: Blue Agave). Accessed June 2018.

http://factpages.npd.no/factpages/default.aspx?culture=en&nav1= wellbore. (Wellbore→ Page view→Exploration→All→24/9-7 A). Accessed June 2018.

Captions

Fig. 1. Outcrop location and lithostratigraphy. a) Location of the study area in the central California. b) Geological map of the Panoche Hills, NW margin of the San Joaquin Valley; red outline is shown in c. c) Geologic map of Right Angle Canyon. The Maastrichtian-Danian stratal units dip ENE with an average dip angle of ca. 30º. A saucer-shaped sandstone intrusion (red) crops out on the NW margin of Right Angle Canyon and cuts the stratigraphy of the Moreno Formation stopping within the Dos Palos Member at the Cima Sandstone Lentil. d) Lithostratigraphy and sandstone intrusion architecture in the study area.

Fig. 2. a) Location of some of the main Paleogene sandstone intrusion complexes (red stars) of the North Sea. b) 3D rendering of the Volund saucer-shaped intrusion from 3D seismic data (modified from Braccini et al., 2006). The lower part of the saucer-shaped intrusion (blue-green) is approximately bedding-parallel (inner sill) whereas bedding-discordant intrusions (dikes) and outer sills define the wings of the intrusion complex (yellow-orange). The depth range between the top of the inner sill and the top of the outer sill is about 240 m. Image x4 vertically exaggerated.

Fig. 3. The saucer-shaped sandstone intrusion in Right Angle Canyon. a) Oblique view (from Google Earth) of Right Angle Canyon (see Fig. 1 for location). b) Geological interpretation of the sandstone intrusion complex. The intensely remobilized parent units are mainly located within the Dosados Member, whereas the sandstone intrusions occur primarily within the Tierra Loma, Marca and Dos Palos members. The upper limit of the injection complex coincides with the Cima Sandstone Lentil, much of which comprises sand extrudites. Saucer-shaped geometry prevails in the thickest sandstone intrusions.

Fig. 4. Lithostratigraphy and petrophysical characteristics. The lithostratigraphy is based on outcrop description whereas borehole log data are from Blue Agave #1 well (see Fig. 1b for location), which has a similar Moreno Fm section to RAC and occurs at a similar depth to Volund field. Average values for bulk density and ultrasonic velocity were used to build the

layered petrophysical model. Shear-wave velocity (Vs) was derived from pressure-wave velocities (Vp).

Table 1

Table shows interval values of ultrasonic velocity and density used in the petrophysical model.

Fig. 5. a) Geological model of Right Angle Canyon (RAC). Sedimentary logs were used for correlation and to define sandstone geometry. Petrophysical characteristics are colour-coded as defined in Table1. b) Equal-angle lower hemisphere stereoplot of the poles of dikes in RAC, n = total number of measurements. Data are corrected for the tectonic dip. c) The seismic survey array as designed in the seismic forward modeller. The target area is located between 1.7 and 2.4 km below the seafloor. d) Synthetic seismic expression of RAC using a zero-phase Ricker wavelet with a peak frequency of 30 Hz. The histogram shows the number of illumination vectors and the maximum dip angle of the reflections illuminated.

Fig. 6. a) The RAC northern wing (see Fig. 3b for location). b) Geological interpretation of a) showing the discordance of the sandstone intrusion and the wedge geometry produced at the intersection between horizontal strata and the intrusion. c) Geological model of the northern wing (see Fig. 5a for location). Minus (-) and plus (+) symbols mark where destructive and constructive wave interference occur, respectively. d) A synthetic seismic model of the northern wing using a zero-phase Ricker wavelet with a peak frequency of 40 Hz to convolve the reflectivity model.

Fig. 7. a) Detail of the RAC southern wing and part of southern inner sill (see Fig. 3b for location). b) Geological interpretation of a) showing the discordance of the sandstone intrusion and the jack-up of the overlying mudstone. c) Geological model of the southern

RAC wing (see Fig. 5a for location). d) Synthetic seismic model of the southern wing using a zero-phase Ricker wavelet with a peak frequency of 40 Hz to convolve the reflectivity model.

Fig. 8. Comparison of actual seismic data with synthetic data in which the horizontal and vertical scales are approximately equal. a) Seismic section through the Volund field saucer-shaped sandstone intrusion (see Fig. 2c for location). The sub-horizontal and stepped high-amplitude reflections are interpreted as part of the inner sill whereas the two main discordant amplitude anomalies occur where the top of the Balder Formation is offset and are interpreted as wings (Huuse et al., 2004; Schwab et al., 2014). Note that emplacement of the inner sill causes jack-up of the overlying strata. Dashed white ovals highlight the occurrence of steps within the inner sill reflections and at the base of the wing reflection as well as amplitude enhancement effect. b) The 40Hz synthetic seismic section from RAC that displays similar geometry to the Volund section. The overall similarity between actual seismic data and synthetic seismic data supports the value of seismic forward modeling of geological models to enhance the seismic interpretation of sandstone intrusions. c) Seismic interpretation of a) showing the main sandstone intrusion features on actual seismic data. d) Seismic interpretation of b) showing the geometry of the saucer-shaped intrusion as a seismic interpreter would see them. e) Geological model of RAC showing the high number of high-angle sandstone intrusions unlikely to be detected by a seismic survey.

Fig. 9 a) Frequency of the sandstone intrusions according to their dip angle. Intrusions that dip at less than ~45° are most likely to be resolved or detected. b) Cross-plot of intrusion thickness against intrusion dip angle. Resolvable, detectable and undetectable fields are defined according to the maximum dip angle illuminated, $\lambda/4$ and $\lambda/30$. A pick frequency of the pulse at the zone of interest of 40Hz, a background velocity of 2000 m/s and an average depth of the target area of 2 km, were used to define the fields as reported in figure. c) Percentage of intrusion thickness interval against the intrusion dip angle. Note that the thickest dikes fall in the range of 10 to 60° with the majority of them below 45°.

Figure 1

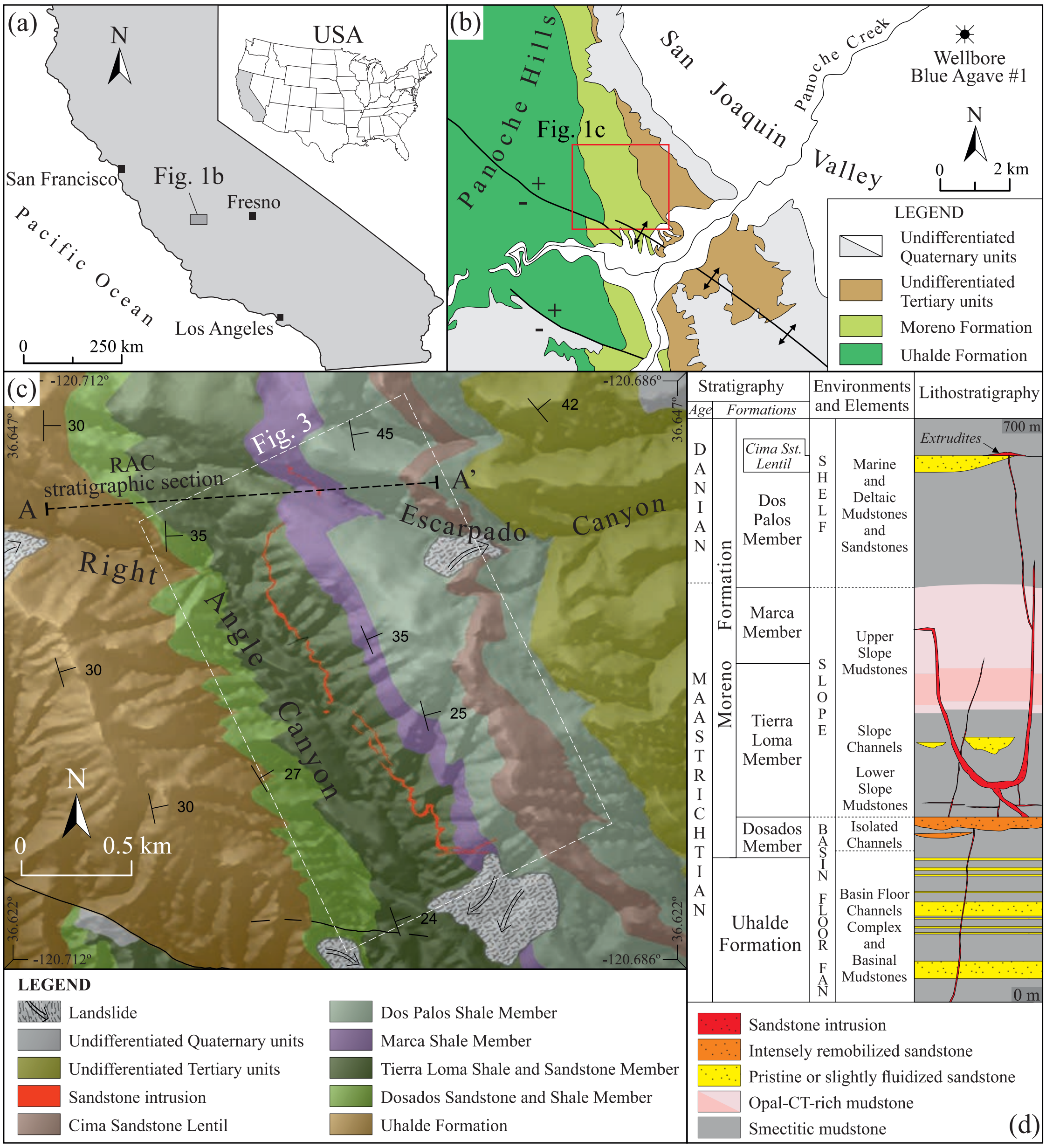

(a)
N
USA
San Francisco
Fig. 1b
Fresno
Pacific Ocean
Los Angeles
0
250 km
(b)
Panoche Hills
Fig. 1c
San Joaquin Valley
Panoche Creek
Wellbore
Blue Agave #1
N
0
2 km
LEGEND
Undifferentiated Quaternary units
Undifferentiated Tertiary units
Moreno Formation
Uhalde Formation
(c)
-120.712º
-120.686º
36.647º
36.622º
Fig. 3
RAC
stratigraphic section
A
A'
Right Angle Canyon
Escarpado Canyon
N
0
0.5 km
LEGEND
Landslide
Undifferentiated Quaternary units
Undifferentiated Tertiary units
Sandstone intrusion
Cima Sandstone Lentil
Dos Palos Shale Member
Marca Shale Member
Tierra Loma Shale and Sandstone Member
Dosados Sandstone and Shale Member
Uhalde Formation
Stratigraphy
Age
Formations
Environments and Elements
Lithostratigraphy
DANIAN
MAASTRICHTIAN
Moreno Formation
Cima Sst. Lentil
Dos Palos Member
Marca Member
Tierra Loma Member
Dosados Member
Uhalde Formation
SHELF
SLOPE
BASIN FLOOR FAN
Marine and Deltaic Mudstones and Sandstones
Upper Slope Mudstones
Slope Channels
Lower Slope Mudstones
Isolated Channels
Basin Floor Channels Complex and Basinal Mudstones
Extrudites
700 m
0 m
Sandstone intrusion
Intensely remobilized sandstone
Pristine or slightly fluidized sandstone
Opal-CT-rich mudstone
Smectitic mudstone
(d)

Figure 2

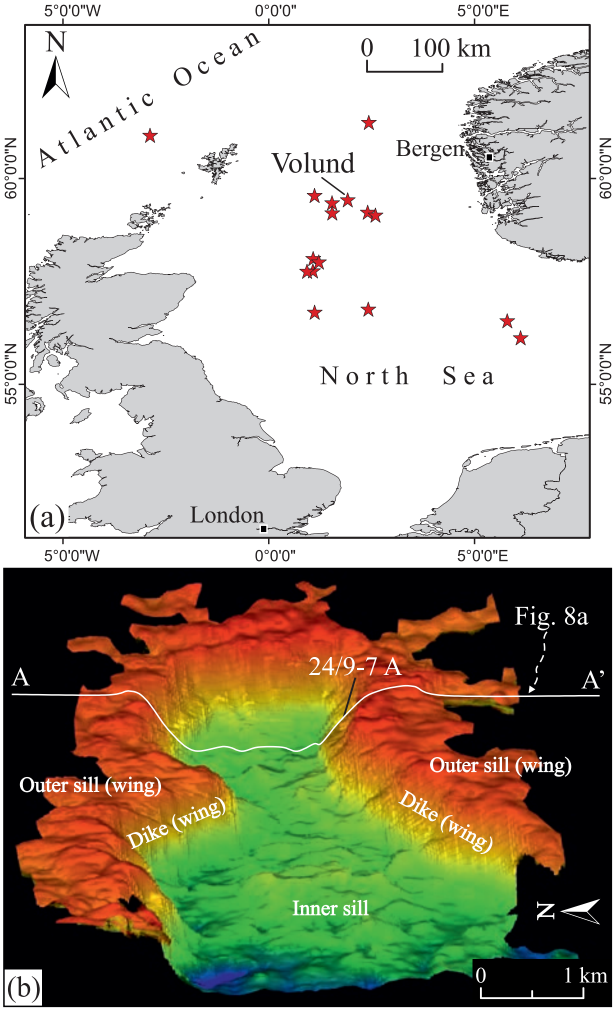

5°0'0"W
0°0'0"
5°0'0"E
N
0
100 km
Atlantic Ocean
Volund
Bergen
60°0'0"N
55°0'0"N
North Sea
London
(a)
Fig. 8a
A
A'
24/9-7 A
Outer sill (wing)
Outer sill (wing)
Dike (wing)
Dike (wing)
Inner sill
N
0
1 km
(b)

Figure 3

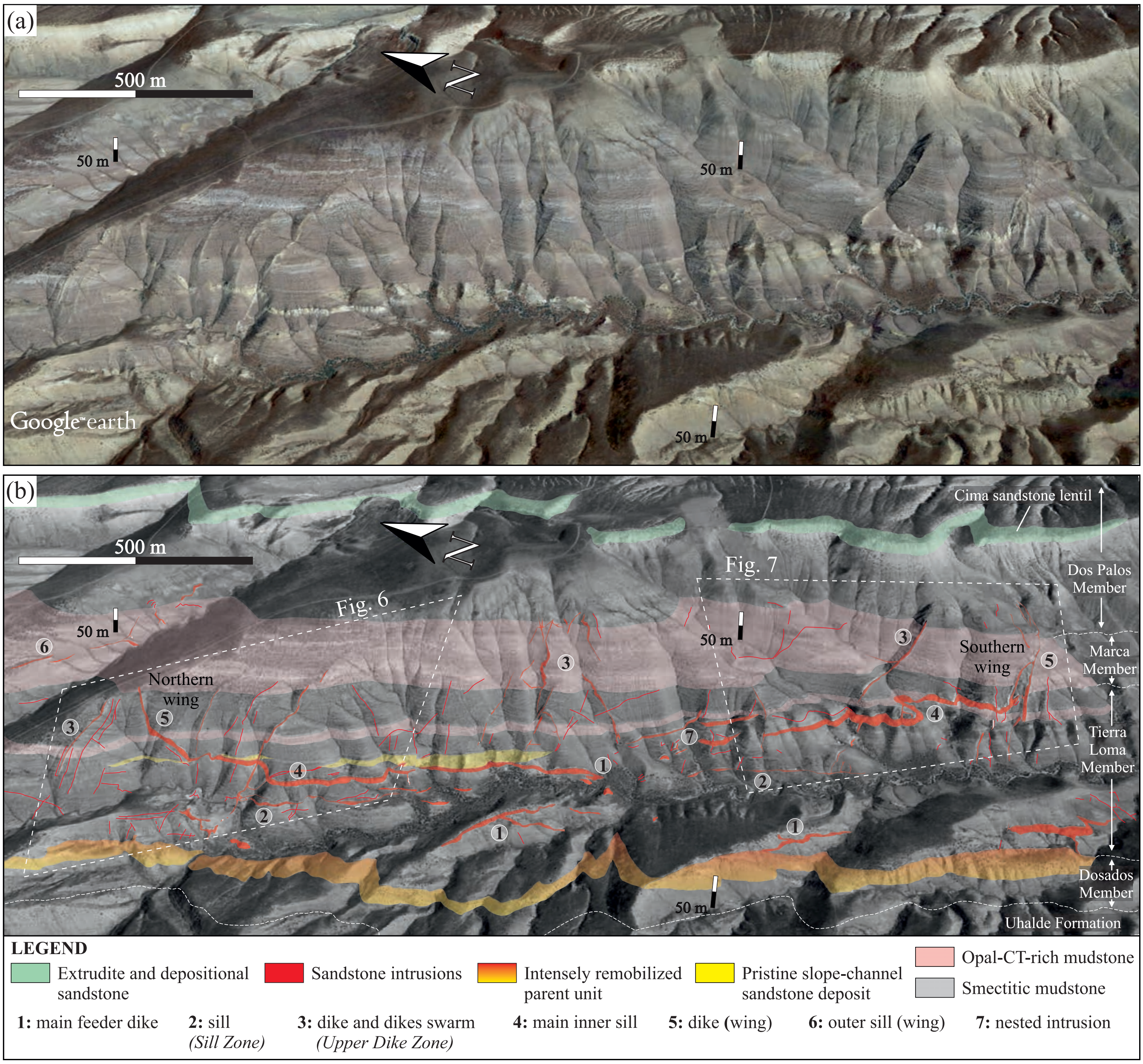
(a)
500 m
N
50 m
50 m
50 m
Google earth
(b)
500 m
N
Cima sandstone lentil
Dos Palos Member
Marca Member
Tierra Loma Member
Dosados Member
Uhalde Formation
Fig. 6
Fig. 7
Northern wing
Southern wing
50 m
50 m
50 m
LEGEND
Extrudite and depositional sandstone
Sandstone intrusions
Intensely remobilized parent unit
Pristine slope-channel sandstone deposit
Opal-CT-rich mudstone
Smectitic mudstone
1: main feeder dike
2: sill (Sill Zone)
3: dike and dikes swarm (Upper Dike Zone)
4: main inner sill
5: dike (wing)
6: outer sill (wing)
7: nested intrusion

Figure 4

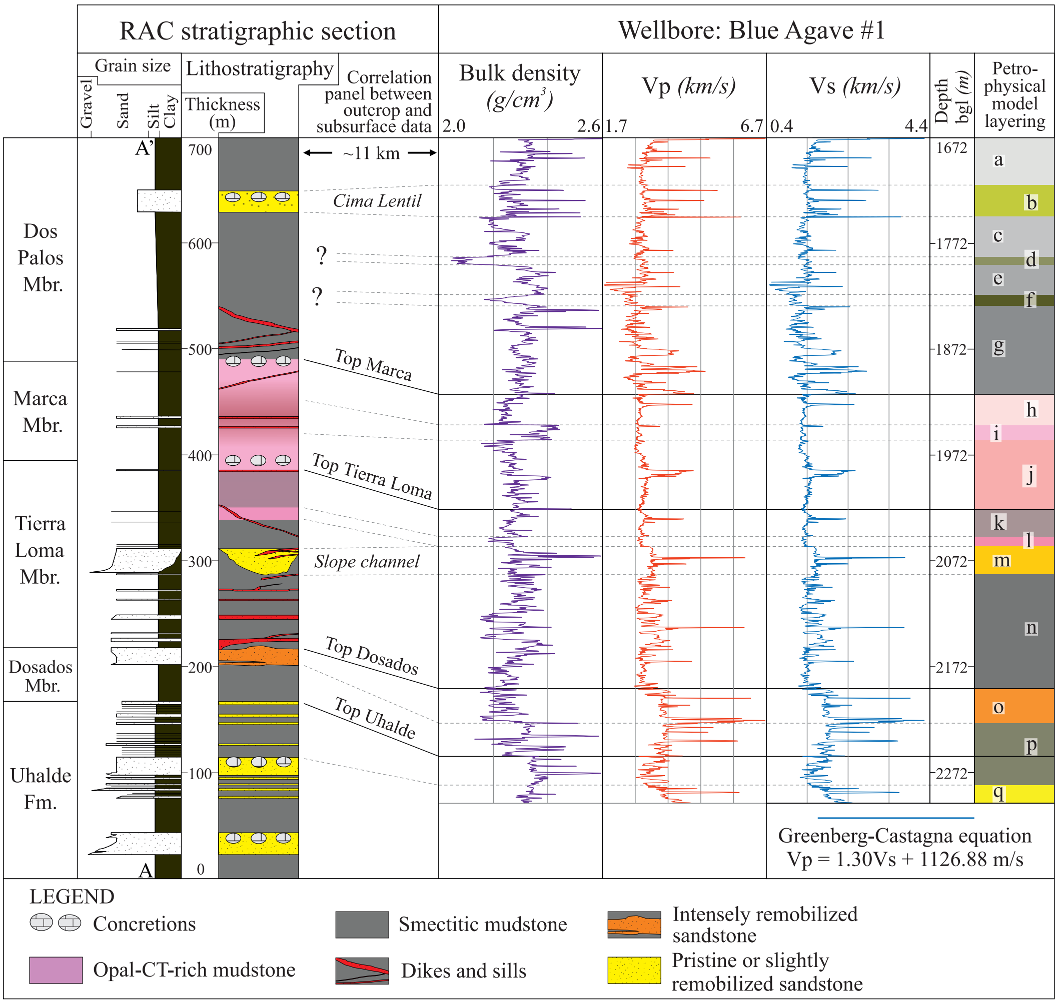

RAC stratigraphic section
Wellbore: Blue Agave #1
Grain size
Gravel
Sand
Silt
Clay
Lithostratigraphy
Thickness (m)
Correlation panel between outcrop and subsurface data
Bulk density (g/cm³)
2.0
2.6
Vp (km/s)
1.7
6.7
Vs (km/s)
0.4
4.4
Depth bgl (m)
Petro-physical model layering
Dos Palos Mbr.
Marca Mbr.
Tierra Loma Mbr.
Dosados Mbr.
Uhalde Fm.
A'
A
700
600
500
400
300
200
100
0
~11 km
Cima Lentil
?
?
Top Marca
Top Tierra Loma
Slope channel
Top Dosados
Top Uhalde
1672
1772
1872
1972
2072
2172
2272
a
b
c
d
e
f
g
h
i
j
k
l
m
n
o
p
q
Greenberg-Castagna equation
Vp = 1.30Vs + 1126.88 m/s
LEGEND
Concretions
Opal-CT-rich mudstone
Smectitic mudstone
Dikes and sills
Intensely remobilized sandstone
Pristine or slightly remobilized sandstone

Tab 1

Data from wellbore Blue Agave #1

Petro-physical model layering	Lithology	Depth bgl *(m)*	Interval values		
			Vp *(m/s)*	**Vs** *(m/s)*	**Rho** *(g/cm³)*
a	smectitic mudstone	1672-1721	3140	1549	2.31
b	silty-sandstone	1721-1747	3212	1604	2.29
c	smectitic mudstone	1747-1784	2853	1328	2.24
d	smectitic mudstone	1784-1791	2895	1360	2.09
e	smectitic mudstone	1791-1820	2761	1257	2.34
f	smectitic mudstone	1820-1831	2585	1122	2.27
g	smectitic mudstone	1831-1914	3010	1449	2.31
h	opal-CT-rich mudstone	1914-1943	2903	1366	2.25
i	opal-CT-rich mudstone	1943-1957	2826	1307	2.38
j	opal-CT-rich mudstone	1957-2023	3014	1452	2.28
k	opal-CT-rich mudstone	2023-2049	2973	1420	2.27
l	opal-CT-rich mudstone	2049-2058	2853	1328	2.24
m	sandstone	2058-2075	3404	1751	2.32
n	smectitic mudstone	2075-2192	3116	1530	2.28
o	sandstone	2192-2224	3834	2082	2.23
p	smectitic mudstone	2224-2256	3770	2033	2.32
q	sandstone	2256-2301	3471	1803	2.36
	concretions	/	5210	3141	2.46

Data from wellbore 24/9-7 A

	Lithology	Depth bsf *(m)*	Interval values		
			Vp *(m/s)*	**Vs** *(m/s)*	**Rho** *(g/cm³)*
sandstone intrusion	Oil-saturated sandstone	1899-1938	2771	1265	2.1

Figure 5

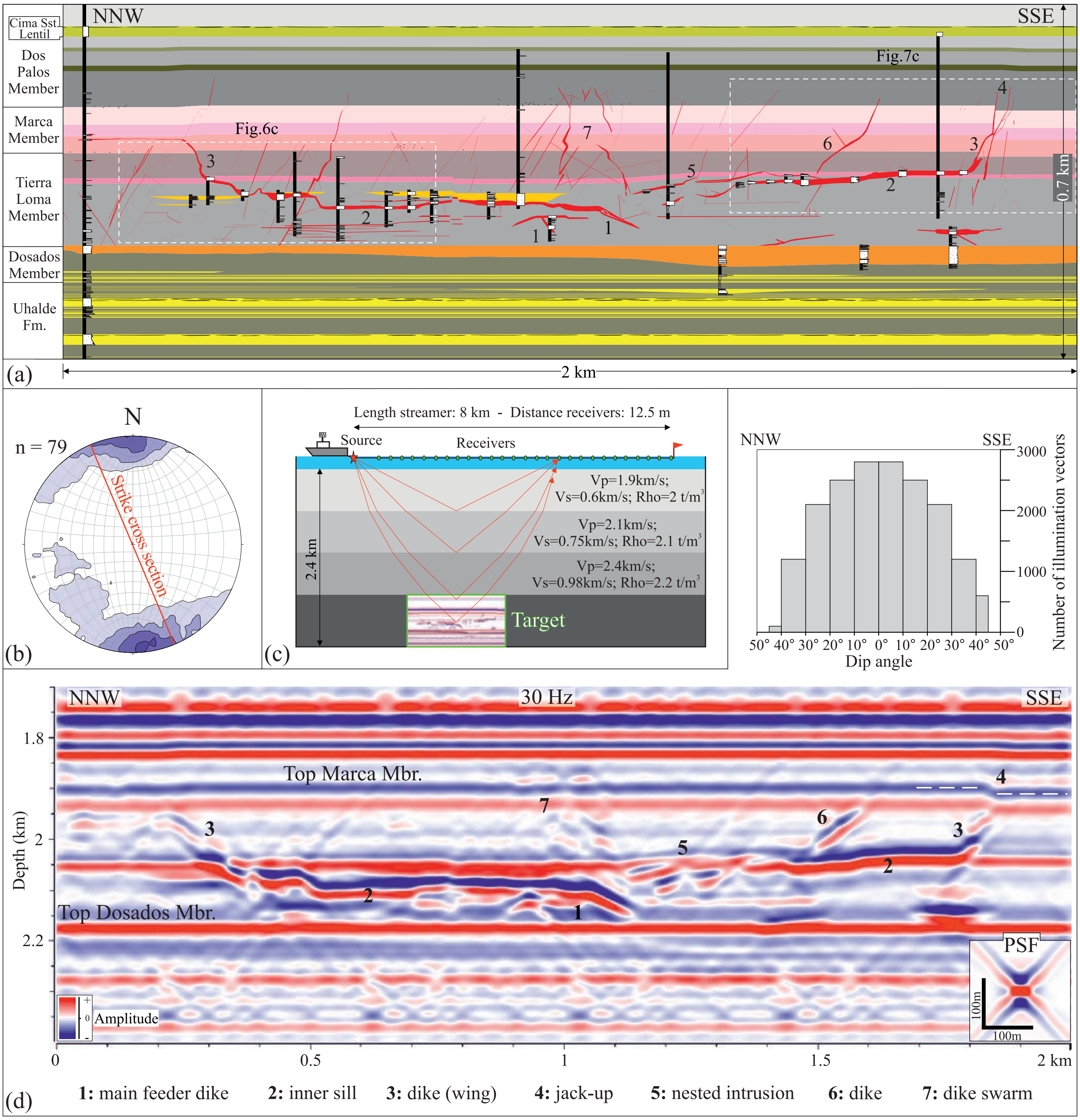
NNW
SSE
Cima Sst. Lentil
Dos Palos Member
Marca Member
Tierra Loma Member
Dosados Member
Uhalde Fm.
Fig.6c
Fig.7c
0.7 km
(a)
2 km
N
n = 79
Strike cross section
(b)
Length streamer: 8 km - Distance receivers: 12.5 m
Source
Receivers
Vp=1.9km/s; Vs=0.6km/s; Rho=2 t/m³
Vp=2.1km/s; Vs=0.75km/s; Rho=2.1 t/m³
Vp=2.4km/s; Vs=0.98km/s; Rho=2.2 t/m³
2.4 km
Target
(c)
NNW
SSE
Number of illumination vectors
Dip angle
30 Hz
Top Marca Mbr.
Top Dosados Mbr.
Depth (km)
Amplitude
PSF
100m
(d)
1: main feeder dike
2: inner sill
3: dike (wing)
4: jack-up
5: nested intrusion
6: dike
7: dike swarm

Figure 6

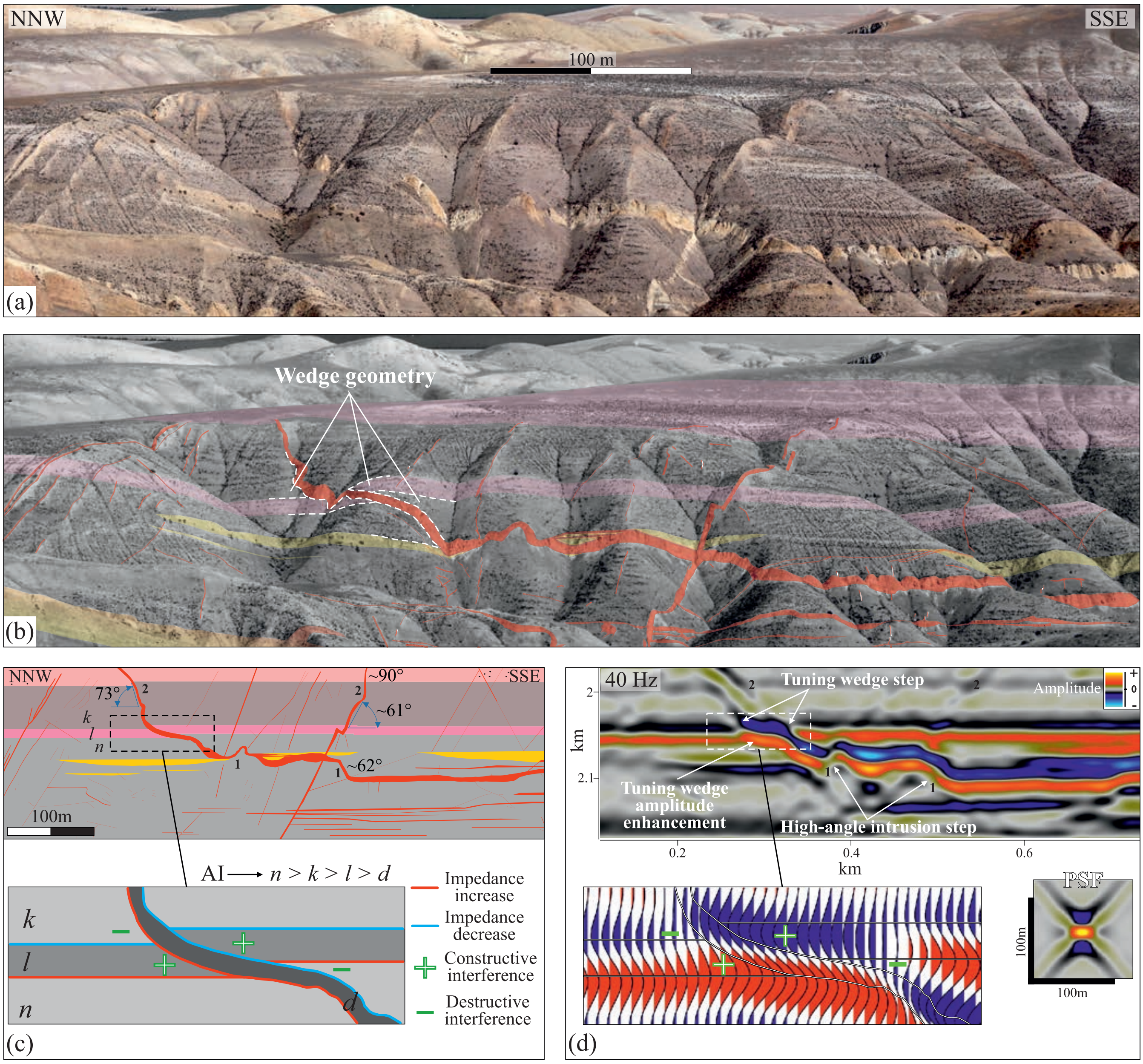

NNW
SSE
100 m
(a)
Wedge geometry
(b)
NNW
SSE
73°
~90°
~61°
~62°
k
l
n
100m
AI ⟶ n > k > l > d
Impedance increase
Impedance decrease
Constructive interference
Destructive interference
(c)
40 Hz
Tuning wedge step
Amplitude
Tuning wedge amplitude enhancement
High-angle intrusion step
km
0.2
0.4
0.6
PSF
100m
(d)

Figure 7

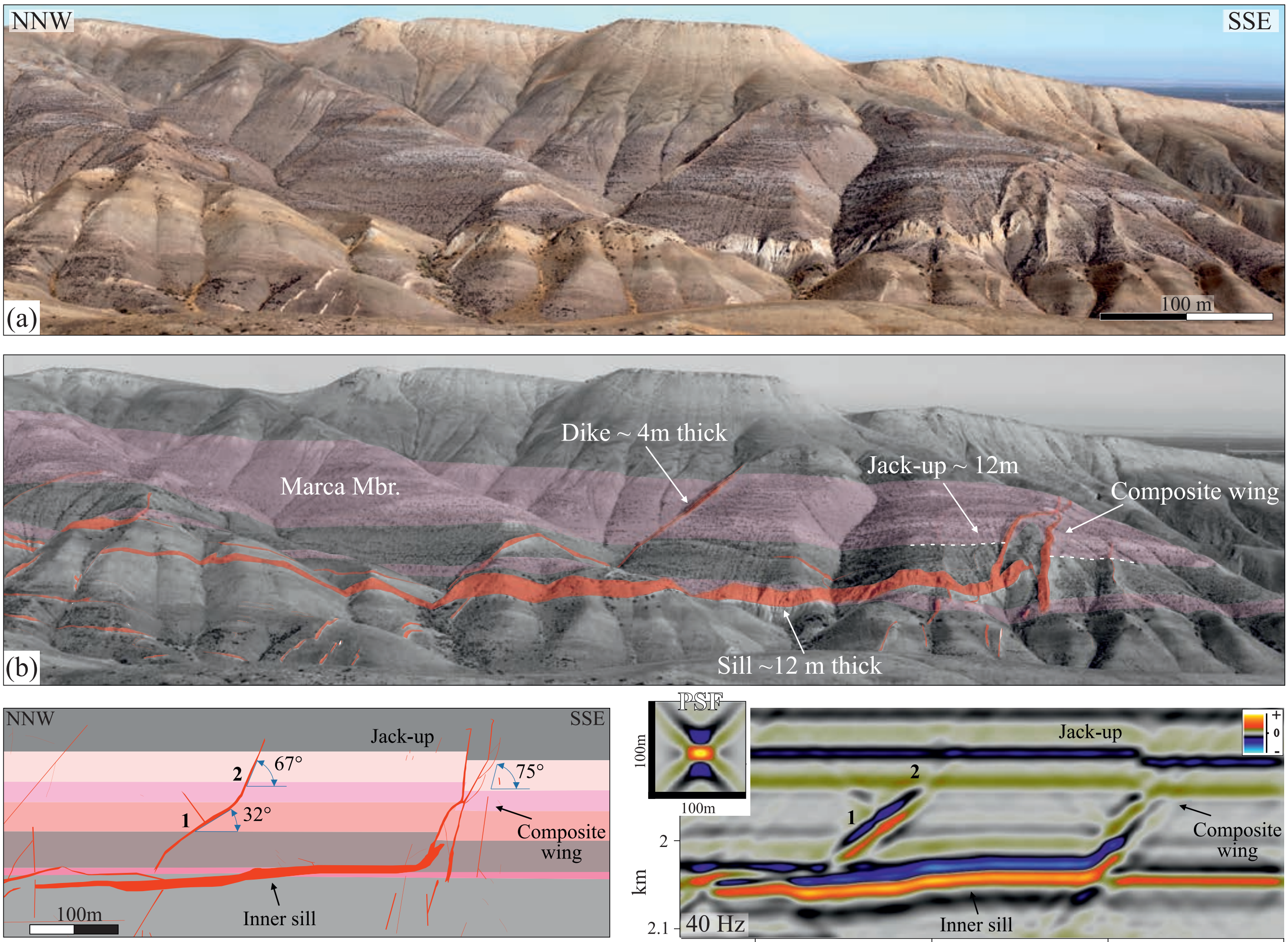

NNW
SSE
100 m
(a)
Marca Mbr.
Dike ~ 4m thick
Jack-up ~ 12m
Composite wing
Sill ~12 m thick
(b)
NNW
SSE
Jack-up
2
67°
1
32°
75°
Composite wing
Inner sill
100m
PSF
100m
100m
Jack-up
+
0
-
2
1
2
km
2.1
40 Hz
Composite wing
Inner sill
1.4
1.6
1.8
2
km

(c)

(d)

Figure 8

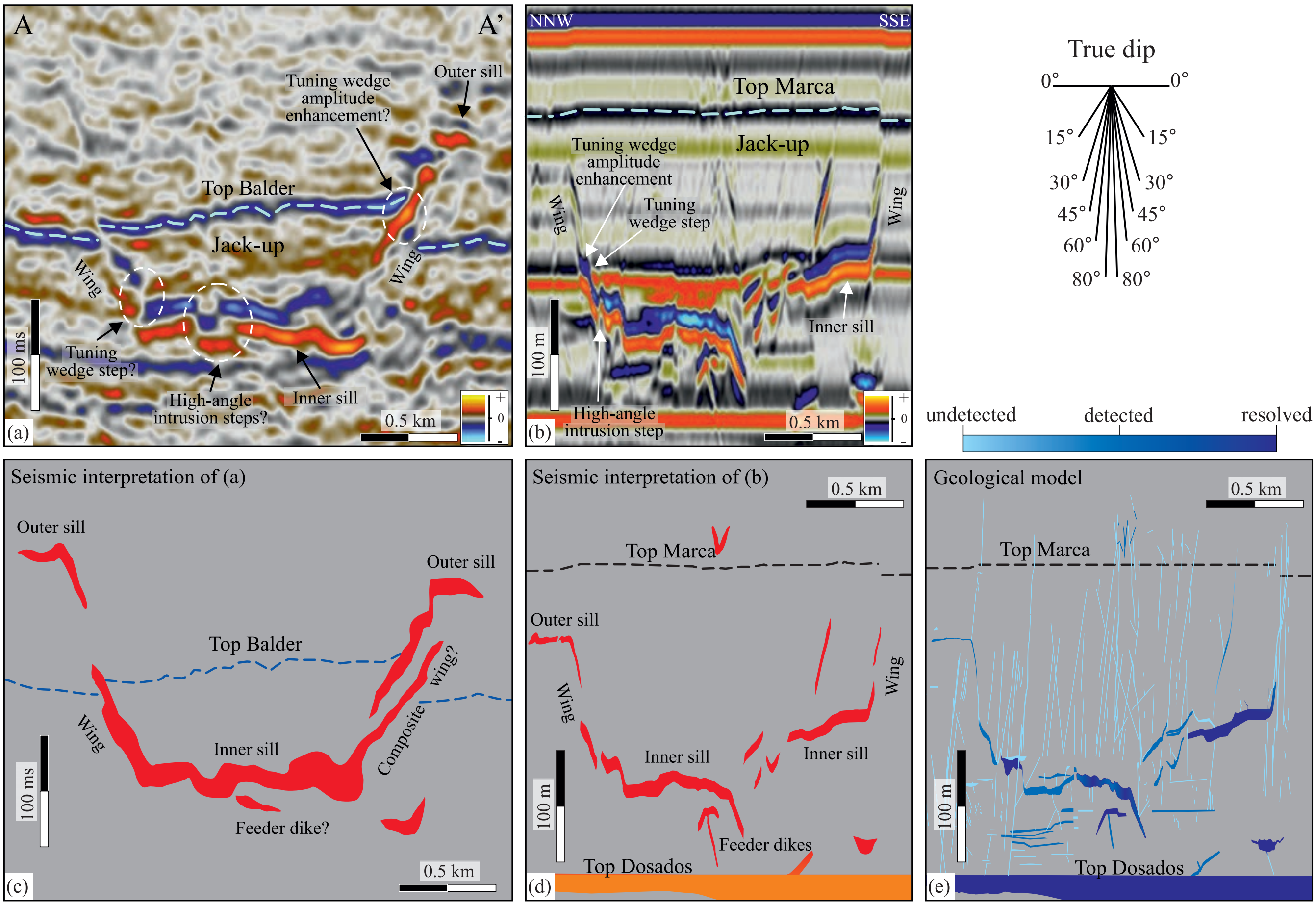
A
A'
Tuning wedge amplitude enhancement?
Outer sill
Top Balder
Jack-up
Wing
Wing
Tuning wedge step?
High-angle intrusion steps?
Inner sill
100 ms
0.5 km
(a)
NNW
SSE
Top Marca
Jack-up
Tuning wedge amplitude enhancement
Tuning wedge step
Wing
Wing
Inner sill
High-angle intrusion step
100 m
0.5 km
(b)
True dip
0°
15°
30°
45°
60°
80°
undetected
detected
resolved
Seismic interpretation of (a)
Outer sill
Outer sill
Top Balder
wing?
Wing
Composite
Inner sill
Feeder dike?
100 ms
0.5 km
(c)
Seismic interpretation of (b)
0.5 km
Top Marca
Outer sill
Wing
Wing
Inner sill
Inner sill
Feeder dikes
Top Dosados
100 m
(d)
Geological model
0.5 km
Top Marca
Top Dosados
100 m
(e)

Figure 9

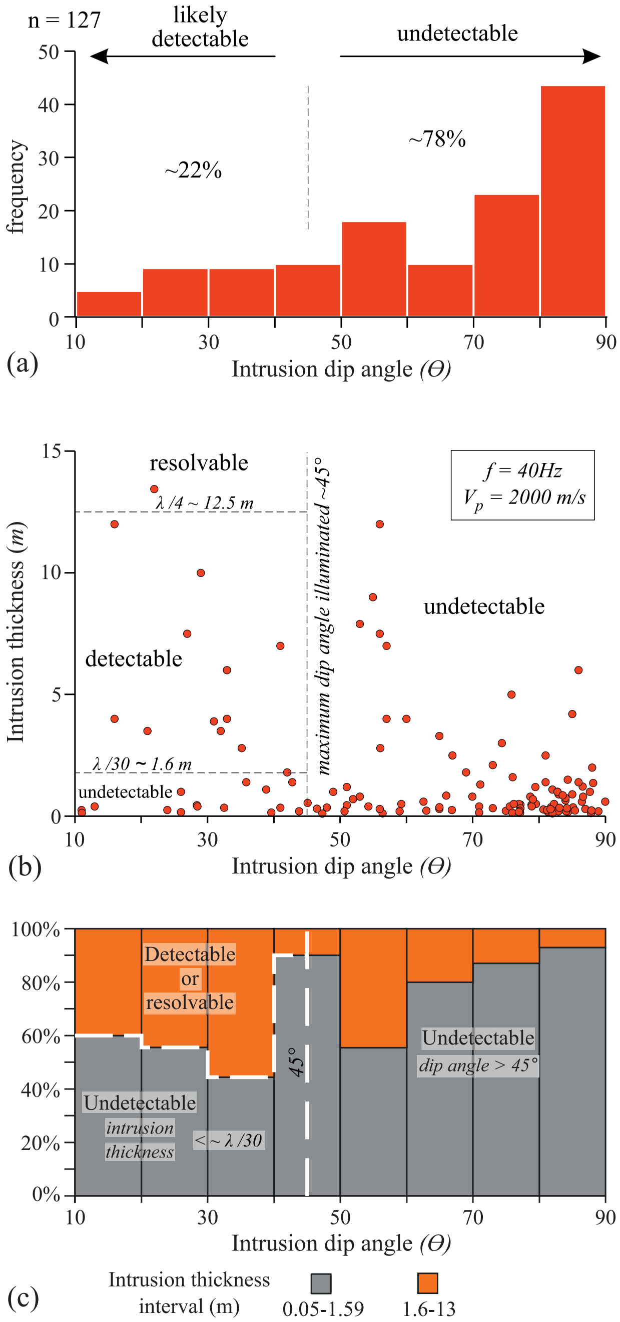

n = 127
likely detectable
undetectable
~22%
~78%
frequency
Intrusion dip angle (Θ)
(a)
resolvable
λ/4 ~ 12.5 m
detectable
λ/30 ~ 1.6 m
undetectable
maximum dip angle illuminated ~45°
undetectable
f = 40Hz
Vp = 2000 m/s
Intrusion thickness (m)
Intrusion dip angle (Θ)
(b)
Detectable or resolvable
Undetectable
intrusion thickness
<~ λ/30
45°
Undetectable
dip angle > 45°
Intrusion dip angle (Θ)
(c)
Intrusion thickness interval (m)
0.05-1.59
1.6-13